



OPEN

Microstructure of porous network $\text{CoFe}_2\text{O}_4@\text{Co}_3\text{O}_4/\text{CNT}$ based on zeolitic imidazolate framework as electrode materials for supercapacitors application

Xiaojun Ding^{1,6}, Dingbang Liu^{1,6}, Zihao Wang², Yilin Peng¹, Shuqi Fu¹, Na Zhan¹, Qing Jiang¹, Mingyang Li¹, Haiyang Wan¹, Jiansheng Liu², Xinsheng Zhao⁴✉, Fei Gao¹✉, Weiping Zhou¹, Zhenzhi Cheng¹, Zhongkai Wu⁵✉ & Guangsheng Luo^{1,3}✉

Transition metal oxides (TMOs), especially spinel-type iron oxides, are widely used as electrode materials for supercapacitors due to their high specific capacitance. However, as a kind of pseudocapacitive electrode material, transition metal oxide undergoes volume changes during the charge–discharge process, leading to a decrease in its cycling stability. Carbon nanotubes (CNTs), as a common carbon-based material, exhibit excellent cycling stability. In this study, we have successfully synthesized $\text{CoFe}_2\text{O}_4@\text{Co}_3\text{O}_4/\text{CNT}$ by utilizing zeolitic imidazolate framework (ZIF) as a template. The resultant material exhibits a porous network architecture and the synthesized material was subsequently utilized as an electrode in supercapacitor applications, exhibiting a remarkable specific capacitance of 641 C g^{-1} at 1 A g^{-1} . The stability of the electrode were evidenced by its ability to retain 62.3% of its initial capacitance after 5000 cycles at the high current density of 10 A g^{-1} , indicating its potential for long-term energy storage applications.

Keywords Supercapacitors, ZIF, CNTs, $\text{CoFe}_2\text{O}_4@\text{Co}_3\text{O}_4\text{-CNT}$, Cycling stability

In the contemporary era, marked by an expanding global population, the severity of energy challenges and concomitant environmental pollution is escalating. To confront these issues, scientific efforts are concentrated on the development of innovative energy storage and conversion devices, such as aluminum-ion batteries¹, magnesium-ion batteries², zinc-ion batteries^{3–7}, and supercapacitors⁸. Compared to other energy storage devices, supercapacitors (SCs) are distinguished by a suite of advantageous properties, including high power density, exceptional cycle stability, and the capacity for rapid charging and discharging processes^{9–12}. Currently, the primary limitations that hinder their widespread practical application are identified as the low energy density, which does not exceed 10 Wh kg^{-1} , and the rate performance, characterized by less than 40% capacitance retention^{13,14}. Recent researches has elucidated that the performance of supercapacitors is largely determined by the chemical composition and physical structure of the materials used for their electrodes¹⁵. As a result, a growing number of researchers are focusing on developing new chemical compositions and innovative structures for electrode materials to improve the electrochemical performance of supercapacitors^{16–19}.

Transition metal oxides, particularly binary transition metal oxides, exhibit superior electrochemical performance compared to monometallic oxide due to the synergistic effect of the two metallic components^{20,21}. Ferrite (MFe_2O_4 , where $\text{M}^{2+} = \text{Co}^{2+}, \text{Mn}^{2+}, \text{Zn}^{2+}, \text{Ni}^{2+}$ et al.) is a prevalent type of binary metal oxide that is recognized for its multiple beneficial attributes such as low cost, environmental sustainability, ample availability

¹School of Physics and Materials, Nanchang University, Nanchang 330031, People's Republic of China. ²School of Advanced Manufacturing, Nanchang University, Nanchang 330031, People's Republic of China. ³Nanjing National Laboratory of Solid State Microstructures, School of Physics, Nanjing University, Nanjing 210093, People's Republic of China. ⁴School of Intelligent Manufacturing Engineering, Jiangxi Institute of Applied Science and Technology, Nanchang 330100, People's Republic of China. ⁵School of Chemistry and Chemical Engineering, Huazhong University of Science and Technology, Wuhan 430074, People's Republic of China. ⁶Xiaojun Ding and Dingbang Liu contribute equally to this work. ✉email: 632403480@qq.com; gaofei@ncu.edu.cn; 1361087131@qq.com; gsluo566@163.com

in natural reserves and excellent electrochemical performance^{22–24}. Consequently, ferrite is often regarded as an ideal material for pseudocapacitive electrodes, holding significant potential for energy storage applications. Up to now, several types of ferrites have been used as high-performance electrode materials for supercapacitors: cobalt ferrite(CoFe_2O_4)²⁵, zinc ferrite(ZnFe_2O_4)²⁶, copper ferrite(CuFe_2O_4)²⁷. Among them, CoFe_2O_4 exhibits an inverse spinel crystal structure, in which Fe^{3+} occupies all the tetrahedral sites and half of the octahedral sites, while Co^{2+} occupies the remaining half of the octahedral sites²⁸. Compared to other types of ferrites, CoFe_2O_4 is distinguished by its exceptional electrical and magnetic properties, which have led to its widespread adoption as an electrode material in supercapacitors^{29,30}. Zeolitic imidazolate frameworks (ZIFs), a class of metal–organic frameworks (MOFs), effectively combine the porous nature of MOFs and the durability of inorganic zeolites^{31,32}. The combination of these features positions ZIFs as favorable precursors for the production of specific compounds, including transition metal oxides (TMOs), transition metal sulfides (TMSs), and transition metal selenides (TMSe)³³. Therefore, integrating ZIF structures into cobalt ferrite can introduce a more extensive array of electrochemical deposition sites and confer unique properties for supercapacitor electrode material. Reddy et al. have successfully synthesized CoS_2 @graphitic carbon/reduced graphene oxide by using ZIF-67 as template³⁴. As the electrode material of supercapacitor, the CoVO-HNC exhibited a maximum specific capacitance of 427.64 F g^{-1} at a current density of 1 A g^{-1} . Despite its merits, CoFe_2O_4 is characterized by certain limitations, including inferior cyclic stability and reduced electrical conductivity, which negatively affect its electrochemical performance³⁵.

Carbon materials are recognized for their widespread application in double-layer capacitors, owing to their exceptional cyclic stability^{36–38}. Among various carbon materials, one-dimensional carbon nanotubes (CNTs) are favored for their long-term cyclic stability as conductors. This is largely due to their strong mechanical properties and efficient electron transport capabilities^{39,40}. Hence, it can be considered that the integration of carbon materials with transition metal oxides offers a viable method for improving the stability of electrode materials in supercapacitors. Cheng et al.⁴¹ successfully synthesized the TCMP electrode by uniformly dispersing CNTs within TOCNs and facile in-situ polymerization of MnO_2 and PANI. The resulting electrode material demonstrated a capacitance retention of approximately 95% after 200 cycles of bending deformation and about 90% after 10 cycles of cutting and repair. Mashkoo et al.⁴² synthesized a novel fCNT-Sm/Co-LDH via the hydrothermal method for the efficient adsorption of antimony (Sb(III)) from wastewater. Following the adsorption process, the antimony-enriched spent adsorbent (fCNT-Sm/Co-LDH@ SbO_3) exhibited remarkable electrochemical performance, achieving a specific capacitance of 850 F g^{-1} at a current density of 2 A g^{-1} . Zhang et al.⁴³ fabricated hierarchical porous carbon materials through a combination of chemical activation and templating methods. The hierarchical porous carbon materials exhibited a high specific capacitance of 380 F g^{-1} at a current density of 0.5 A g^{-1} , along with commendable cycling stability, retaining 93% of their capacitance after 10,000 consecutive charge–discharge cycles at a current density of 5 A g^{-1} .

In this study, we synthesize CoFe_2O_4 @ Co_3O_4 by using the ZIFs as a template. By varying the mass of CNTs, we have successfully synthesized a series of CoFe_2O_4 @ Co_3O_4 /CNT- x ($x = 50, 100, 150, 200, 250 \text{ mg}$), where x represents the mass of CNTs. Among all of CoFe_2O_4 @ Co_3O_4 /CNT- x , the CoFe_2O_4 @ Co_3O_4 /CNT-100 with porous network structure exhibited the highest specific capacitance of 641 C g^{-1} at a current density of 1 A g^{-1} and excellent rate performance of 69% from 1 A g^{-1} to 10 A g^{-1} . The results indicated that CoFe_2O_4 @ Co_3O_4 /CNT-100 has the potential to be used as the electrode material for supercapacitor with high specific capacitance and excellent cyclic stability.

Experimental

Chemicals and apparatus

All reagents used in this study were of analytical grade and required no further purification. The chemicals used include cobalt nitrate hexahydrate [$\text{Co}(\text{NO}_3)_2 \cdot 6\text{H}_2\text{O}$], ferrous sulfate [$\text{Fe}(\text{SO}_4)_2 \cdot 7\text{H}_2\text{O}$], benzimidazole ($\text{C}_7\text{H}_6\text{N}_2$), carbon nanotube (CNTs) potassium hydroxide (KOH), hydrochloric acid (HCl), polyvinyl pyrrolidone (PVP), N,N-Dimethylformamide (DMF), and methanol (CH_3OH). These chemicals were obtained from Aladdin Industrial Co. Ltd. Activated carbon (AC) was sourced from Sinopharm. Nickel foam (NF) with a thickness of 0.5 mm and an open porosity of 97.2% was acquired from Changde Liyuan Metal Materials Co, Ltd.

Synthesis of CoFe-ZIF@CNT-100

The preparation process of CoFe-ZIF@CNT-100 is illustrated in Fig. 1. CoFe-ZIF@CNT-100 was synthesized using a simple hydrothermal method. We select the optimal ratio of Co^{2+} to Fe^{2+} (3:1)⁴⁴. Firstly, 50 mg of CNTs and 0.4 g of PVP were dissolved in 30 ml DMF. The resulting solution was ultrasonicated for 30 min to ensure a uniform dispersion of CNTs in the DMF solution, denoted as Solution A. Next, 0.417 g (1.5 mmol) $\text{Fe}(\text{SO}_4)_2 \cdot 7\text{H}_2\text{O}$ and 1.3096 g (4.5 mmol) $\text{Co}(\text{NO}_3)_2 \cdot 6\text{H}_2\text{O}$ were dissolved in 30 ml DMF, followed by ultrasonic and stirring for 5 min respectively to obtain Solution B. Solution B was slowly poured into Solution A then ultrasonicated for 30 min to obtain a homogeneous suspension. Subsequently, 2.83 g of $\text{C}_7\text{H}_6\text{N}_2$ were introduced into the mixture solution, which was then subjected to ultrasonication for a period of 5 min. The mixed solution was transferred to a Teflon-lined stainless steel autoclave of 100 ml capacity and subjected to a hydrothermal reaction at 180°C for 24 h. Afterward, the solution obtained from the hydrothermal reaction was filtered, washed twice with methanol and deionized water respectively. The obtained black powder was referred to CoFe-ZIF@CNT-100. For comparison purposes, CoFe-ZIF@CNTs with different mass of CNTs (50, 150, 200, 250 mg) were synthesized following the same procedure and conditions. The samples with different mass of CNTs are named as CoFe-ZIF@CNT- x ($x = 50, 100, 150, 200, 250$, representing the mass of CNTs).

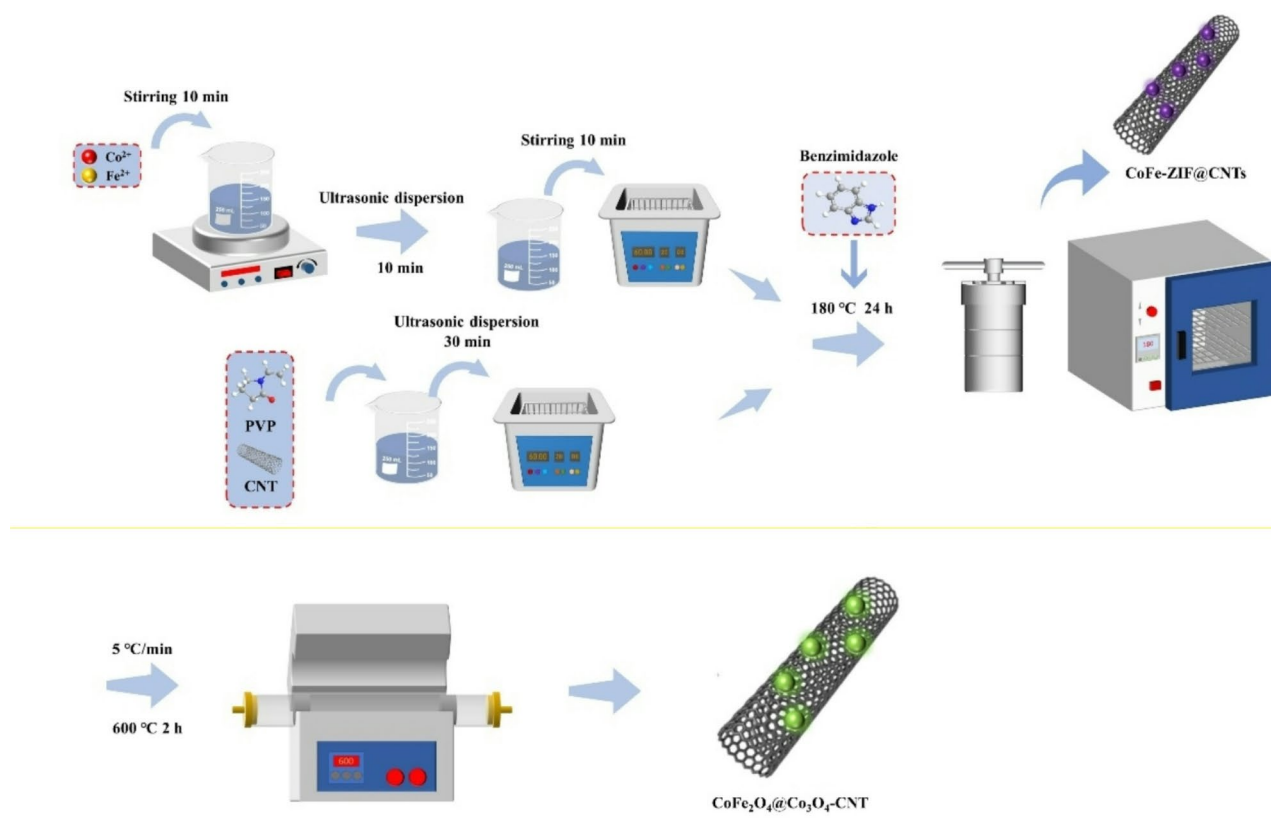


Fig. 1. Schematic illustration for the preparation process of FCO@CNT-100.

Synthesis of flower-like spherical $\text{CoFe}_2\text{O}_4@ \text{Co}_3\text{O}_4/\text{CNT-100}$

In a typical synthetic process, the obtained black powder was placed into a tubular furnace and heated at a rate of $5^\circ\text{C}/\text{min}$ under the Ar atmosphere until reaching 600°C . It was then maintained at this temperature for 2 h before cooling naturally to room temperature. The obtained black powder was labeled as $\text{CoFe}_2\text{O}_4@ \text{Co}_3\text{O}_4/\text{CNT-100}$. By keeping the concentration ratio of Co^{2+} to Fe^{2+} constant, the mass of CNTs was varied (50 mg, 100 mg, 150 mg, 200 mg, 250 mg). The samples with different mass of CNTs are named as $\text{CoFe}_2\text{O}_4@ \text{Co}_3\text{O}_4/\text{CNT-x}$ ($x=50, 100, 150, 200, 250$, representing the mass of CNTs). For the sake of simplicity, the resulting products were labeled as FCO@CNT- x ($x=50, 100, 150, 200, 250$, representing the mass of CNTs).

Characterization

X-ray diffraction (XRD) analysis was performed using a Bruker D8 ADVANCE powder X-ray diffractometer with Cu-K α radiation ($\lambda=1.54056 \text{ \AA}$). The structure of the electrode materials was examined using a Hitachi SU8100 scanning electron microscope (SEM) equipped with a PW9900 energy-dispersive X-ray spectroscopy (EDS) system. Transmission electron microscopy (TEM) imaging was carried out using a JEOL JEM-2100 high-resolution transmission electron microscope operating at 200 kV. The Raman spectra was tested by a Raman spectrometer (HORIBA Scientific LabRAM HR Evolution). The surface area of the samples was determined using the BET method, while the porosity was calculated using the BJH model. X-ray photoelectron spectroscopy (XPS) measurements were carried on an ESCALAB250 with an Al target K α ray radiation source.

Electrochemical test

Before the electrochemical test, the Ni foam (NF) electrode, which was 1 cm in diameter, underwent pretreatment to rid its surface of any present grease and oxides. This involved putting the NF through a stepwise ultrasonic cleaning in diluted hydrochloric acid, followed by ethanol, and finally deionized water, with the objective of purifying the NF surface from any contaminants. After cleaning, the NF was dried in a vacuum at 70°C all through the night to get rid of any lingering moisture and solvents. For the electrochemical investigations within this research, a three-electrode system was employed, including a working electrode composed of the manufactured products, a counter electrode made of platinum, and a Hg/HgO reference electrode. The creation of the working electrode adhered to a defined process. This began with dispersing the created products alongside acetylene black and polyvinylidene fluoride (PVDF) in an N-methylpyrrolidone (NMP) solution by ultrasonication, keeping the component mass ratio at 7:1.5:1.5. Afterward, this blend was evenly applied to the pristine, dry NF. This coated NF was again placed under vacuum drying at 70°C for the entire night. The ultimate step involved the pressing of the dried NF into sheets, forming the working electrodes for the forthcoming tests.

The electrochemical assessments were conducted at an electrochemical station (CHI660E, Shanghai), including cyclic voltammetry (CV), galvanostatic charge–discharge (GCD) tests, and electrochemical impedance spectroscopy (EIS) spanning a frequency range from 0.01 to 100 kHz at the open circuit potential. Within the three-electrode array and using a 3 M KOH solution, CV was tested over diverse scanning rates (10, 30, 50, 80, 100 mV s⁻¹), GCD was measured across varying current densities (1, 3, 5, 8, 10 A g⁻¹). The mass-specific capacitances for the electrode material at the different current densities were determined using the GCD curves by:

$$C_{sp} = \frac{I\Delta t}{m} \quad (1)$$

In the formula, C_{sp} (C g⁻¹) signifies the specific capacitance of electrode material, I (A) denotes the charge and discharge current, m (g) indicates the mass of active material, ΔU (V) is the voltage window, and Δt (s) is the discharge time.

Results and discussion

The preparation process of CoFe-ZIF@CNT-100 is illustrated in Fig. 1. CoFe-ZIF@CNT-100 was synthesized using a simple hydrothermal method. The quantity of carbon nanotubes (CNTs) substantially influences the electrochemical performance of electrode materials. The X-ray diffraction (XRD) patterns of CoFe-ZIF@CNTs is presented in Fig. S1. The presence of CoO₂ (indexed as no. 89-8399) and Fe₂O₃ (indexed as no. 89-7047) in the hydrothermal process, particularly in the mass of CNT of 100 mg. To study the phase constitution of the prepared ferrite cobalt oxide coated with carbon nanotubes (FCO@CNTs), X-ray diffraction (XRD) technology was employed for characterization. Figure 2a presents the XRD pattern of FCO@CNTs, which includes several diffuse peaks corresponding to carbon nanotubes and CoFe₂O₄. Moreover, The peak at 54° can be attributed to the CNTs as it is seen that the intensity of this peak increases with CNT loading in the sample, which further prove the successful synthesis of our prepared samples. Among the samples prepared with varying masses of carbon nanotubes (CNTs), FCO@CNT-100 is distinguished by the sharpest peaks, which suggests superior crystallinity in comparison to the other samples. Co₃O₄ and Fe₂O₃ are two common by-products in the synthesis of cobalt-based ferrite. The peak corresponding to the (111) plane can be matched with the standard PDF card of carbon (PDF#99-0043), with its 2θ angle located at 44.295°. The peak for the (116) plane corresponds to Fe₂O₃ (PDF#74-2120), with its 2θ angle at 54.002°. This observation suggests that the carbon nanotubes have been effectively coated onto the surface of the cobalt-based ferrite, denoted as FCO@CNTs.

Preliminary assessments from X-ray diffraction (XRD) analysis indicate the successful deposition of carbon nanotubes (CNTs) onto the cobalt-based ferrite. To gain further insights into the carbonaceous composition within the composite, as well as to evaluate the degree of structural order and the presence of any crystal defects, Raman spectroscopic analysis was conducted on the FCO@CNT-100 sample, as depicted in Fig. 2b. The two peaks observed at 1344 cm⁻¹ and 1577 cm⁻¹ in the figure are characteristic peaks belonging to CNTs, and the peaks at 663 cm⁻¹ can be attributed to CoFe₂O₄⁴⁴, which further proving the formation of cobalt-based ferrite in the composite material. The D peak is associated with highly ordered graphite lattices, while the G peak is related to sp²-bonded carbon. Typically, the intensity ratio of the D peak to the G peak (I_D/I_G) in Raman spectroscopy is utilized to ascertain the density of defects within a material^{45,46}. The I_D/I_G ratio, which is commonly around 0.8 for multiwalled carbon nanotubes (CNTs), serves as an indicator of the defect density within carbon-based materials (as shown in Fig. S2). In the case of FCO@CNT-100, the I_D/I_G ratio is measured to be 0.803.

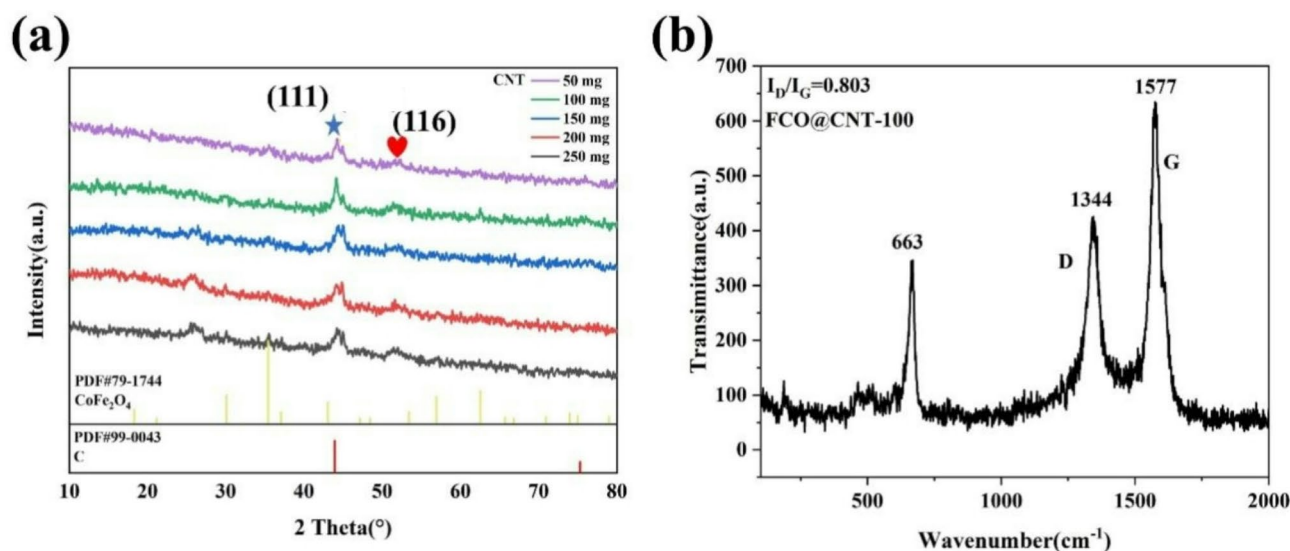


Fig. 2. (a) XRD patterns of FCO@CNTs with different mass of CNTs; (b) Raman spectra of FCO@CNT-100.

The morphological structure of FCO@CNT-100 was examined using scanning electron microscopy (SEM) and high-resolution transmission electron microscopy (HRTEM) to obtain images at different magnifications. As shown in Fig. 3a, FCO@CNT-100 exhibits a microsphere-like shape with a diameter of approximately 3 μm . The TEM analyses in Fig. 3b,c revealing that the synthesized microspheres exhibit a heterogeneous size distribution ranging from 3 μm to 10 μm . The observed size disparity is ascribed to heterogeneous nucleation during the hydrothermal reaction, driven by temperature gradients and inconsistencies in the initial grain size. Additionally, the TEM images distinctly demonstrate the presence of abundant carbon nanotube structures adjacent to the microspheres, consistent with the composite architecture depicted in the schematic diagram in Fig. 1. The combined analysis of Fig. 3 suggests that these tubular structures are protruding from the microsphere surface, indicating the presence and integration of carbon nanotubes (CNTs) within the FCO@CNT-100 microspheres. Figure 3b,c present TEM images that further illustrate the interconnection of the nano-spheres via CNTs, forming a three-dimensional (3D) porous network structure. This network structure is critical for the material's enhanced electrochemical performance, as it facilitates efficient ion and electron transport pathways—key factors for achieving high specific capacitance and rate performance. However, the TEM images also suggest that an excess of CNTs can lead to aggregation, potentially trapping cobalt-based ferrite particles. This aggregation may significantly reduce the material's surface area in contact with the electrolyte solution, thereby adversely affecting the specific capacitance of the electrode material. Agglomeration of carbon nanotubes (CNTs) reduces the effective surface area in contact with the electrolyte, hampers ion accessibility, and impedes electron transfer, thereby lowering the overall efficiency of the electrode. This inference is supported by the observed decline in specific capacitance as the CNT content exceeds 100 mg and continues to increase. Regarding the concern that larger microspheres may be suboptimal for electrode materials due to reduced electrolyte accessibility and compromised structural integrity, we would like to emphasize that the porous network formed by the CNTs

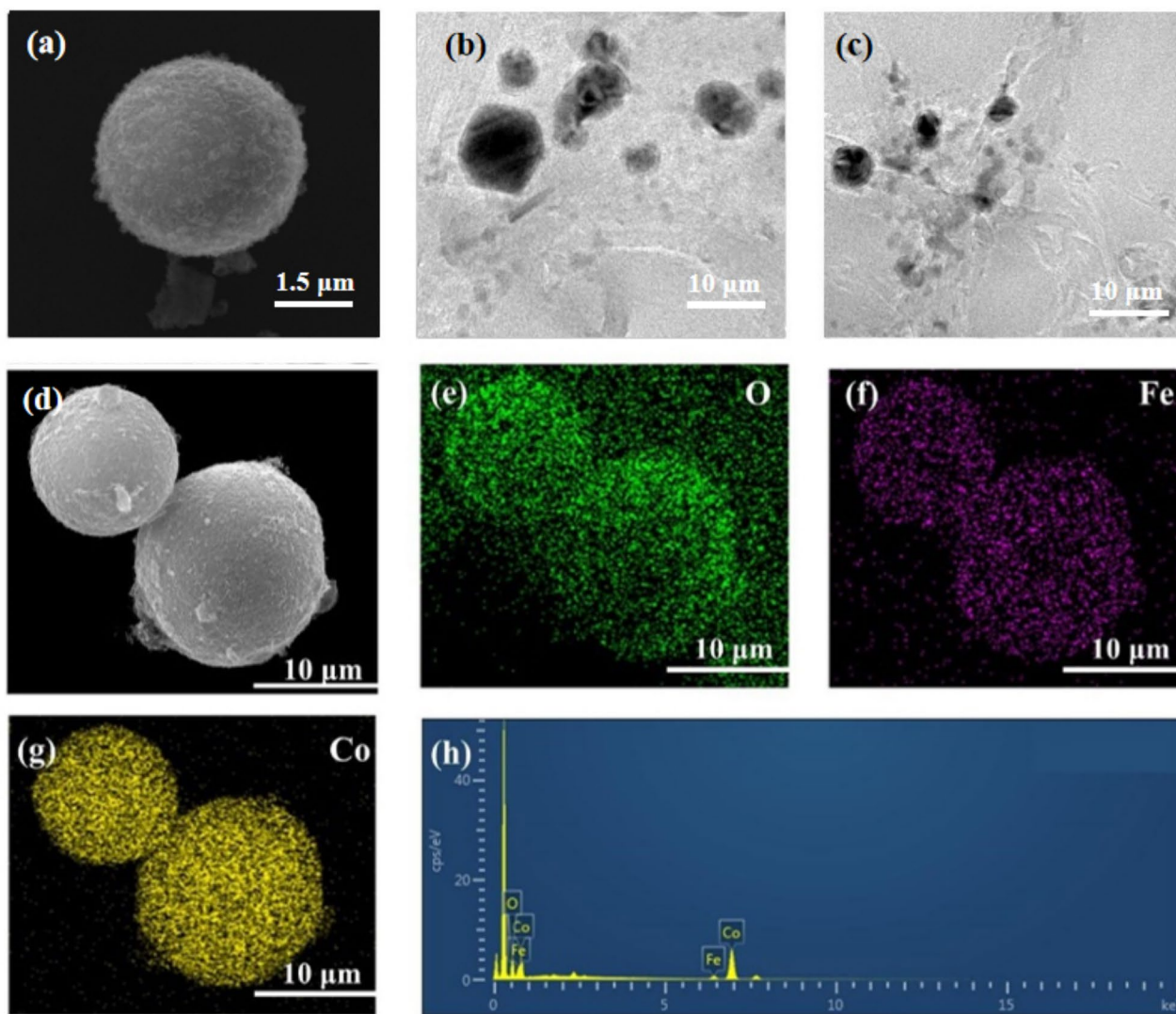


Fig. 3. (a,b)SEM images of FCO@CNT-100; (c,d)TEM images of FCO@CNT-100; (e–h) EDS elements mapping of FCO@CNT-100.

effectively mitigates these potential drawbacks. The interconnected CNTs not only enhance the mechanical stability of the structure but also provide additional pathways for electrolyte penetration, thereby improving the overall electrochemical performance despite the larger microsphere size. Additionally, Fig. 3e–h display the Energy-Dispersive X-ray Spectroscopy (EDS) spectrum of FCO@CNT-100, confirming the presence and uniform distribution of cobalt (Co), iron (Fe), and oxygen (O) elements across the microspheres. Table S1 demonstrated the mass ratio of Co, Fe and O.

In order to analyze the valence states of the elements within FCO@CNT-100, we conducted X-ray photoelectron spectroscopy (XPS) analysis on the sample, as depicted in Fig. S3. As illustrated in Fig. S3(a), the XPS spectra confirmed the presence of Co, Fe, O, C, and N elements in the sample. The signal for the N element may originate from residual organic ligands, while the signal for the C element is attributed to the carbon nanotubes. Fig. S3(b) presents the high-resolution XPS spectra of the Fe 2p orbitals. The Fe 2p spectra exhibit two spin-orbit doublets (Fe 2p_{1/2} and Fe 2p_{3/2}) and two satellite peaks (Sat.). The binding energies observed at 708.28 eV and 717.21 eV can be assigned to Fe 2p_{3/2} and Fe 2p_{1/2} of Fe²⁺, respectively, while the peaks observed at 711.35 eV and 722.59 eV correspond to Fe 2p_{3/2} and Fe 2p_{1/2} of Fe³⁺. Fig. S3(c) presents the high-resolution XPS spectra of the Co 2p orbitals. The Co 2p_{3/2} and Co 2p_{1/2} spectra exhibit distinct spin-orbit doublets and shake-up satellites, corresponding to the characteristic peaks of Co²⁺ (780.04 eV and 795 eV) and Co³⁺ (776.7 eV and 791.7 eV), respectively. Additionally, Fig. S3(d) displays the high-resolution spectra of O 1s. The signals observed at 528.3 eV can be attributed to M²⁺-O bonds (where M²⁺ represents Co²⁺ and Fe²⁺), where the signals observed at 530 eV may arise from M³⁺-O (M³⁺ = Co³⁺, Fe³⁺).

To ascertain the optimal quality of carbon nanotubes (CNTs), electrochemical evaluations including CV and GCD was performed on all synthesized electrode materials within a three-electrode test configuration. The mass loading of electrodes are demonstrated in Table S2. The CV tests were executed at a scanning rate of 10 mV s⁻¹, while the GCD measurements were performed at a current density of 1 A g⁻¹ using a 3 M KOH electrolyte solution to examine the electrochemical properties of CoFe-ZIF@CNTs. 3M is an appropriate concentration, which can not only ensure enough electrolyte ions dissolution/dissociation, but also prevent the negative impact of too high concentration on the device, consequently, 3M is chosen for the subsequent measurements^{47–50}. Figure 4a presents the CV curves of CoFe-ZIF@CNTs at the specified scan rate. Observations from the electrochemical tests reveal that each product manifests sharp and distinct redox peaks throughout the electrochemical process, a phenomenon that is indicative of active faradaic oxidation–reduction reactions. The presence of these peaks corroborates the occurrence of a reversible electrochemical process within the CoFe-ZIF@CNTs samples. Among the variants, CoFe-ZIF@CNT-100 demonstrated the most pronounced redox peaks and the largest CV curve area, suggesting a higher specific capacitance compared to other CoFe-ZIF@CNT compositions. Figure 4b displays the GCD curves of CoFe-ZIF@CNTs at a current density of 1 A g⁻¹. It is observed that CoFe-ZIF@CNT-100 exhibits the longest discharge time, which is directly proportional to its specific capacitance. Figure 4c illustrates the calculation of specific capacitance for CoFe-ZIF@CNTs using the formula (1), where CoFe-ZIF@CNT-100 is determined to have the highest specific capacitance value of 72 C g⁻¹. A notable decrease in specific capacitance is observed when the CNT mass is increased from 100 to 150 mg. Beyond this point, as the CNT mass increases from 150 to 250 mg, the specific capacitance decline is less pronounced. This trend may be attributed to the agglomeration of excess CNTs, which could hinder the accessibility of active sites, while the double-layer capacitance contribution from the CNTs remains significant.

Following a calcination process at 600 °C for 2 h in an argon (Ar) atmosphere, the carbon framework of CoFe-ZIF@CNTs undergo structural variation, resulting in the formation of FCO@CNTs. To evaluate the electrochemical performance of the resultant FCO@CNTs, a series of electrochemical tests were conducted using a three-electrode test system. The mass loading of electrodes are demonstrated in Table S3. Figure 5a presents the cyclic voltammetry (CV) curves for FCO@CNT-x, where x represents varying masses of carbon nanotubes (50, 100, 150, 200, and 250 mg) at a scan rate of 10 mV s⁻¹. Examination of the CV curves reveals that all FCO@CNT samples exhibit a distinct pair of redox peaks, which are indicative of the faradaic oxidation–reduction reactions associated with the Co²⁺/Co³⁺ and Fe²⁺/Fe³⁺ couples^{51,52}.

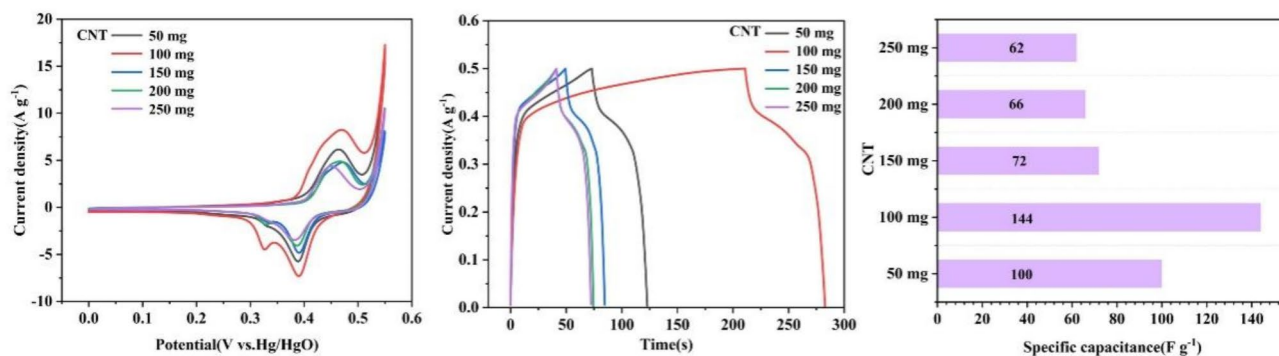


Fig. 4. (a) CV curves of CoFe-ZIF@CNTs with different mass of CNTs at the scanning rate of 10 mV s⁻¹; (b) GCD curves of CoFe-ZIF@CNTs with different mass of CNTs at a current density of 1 A g⁻¹; (c) Specific capacitance of CoFe-ZIF@CNTs with different mass of CNTs.

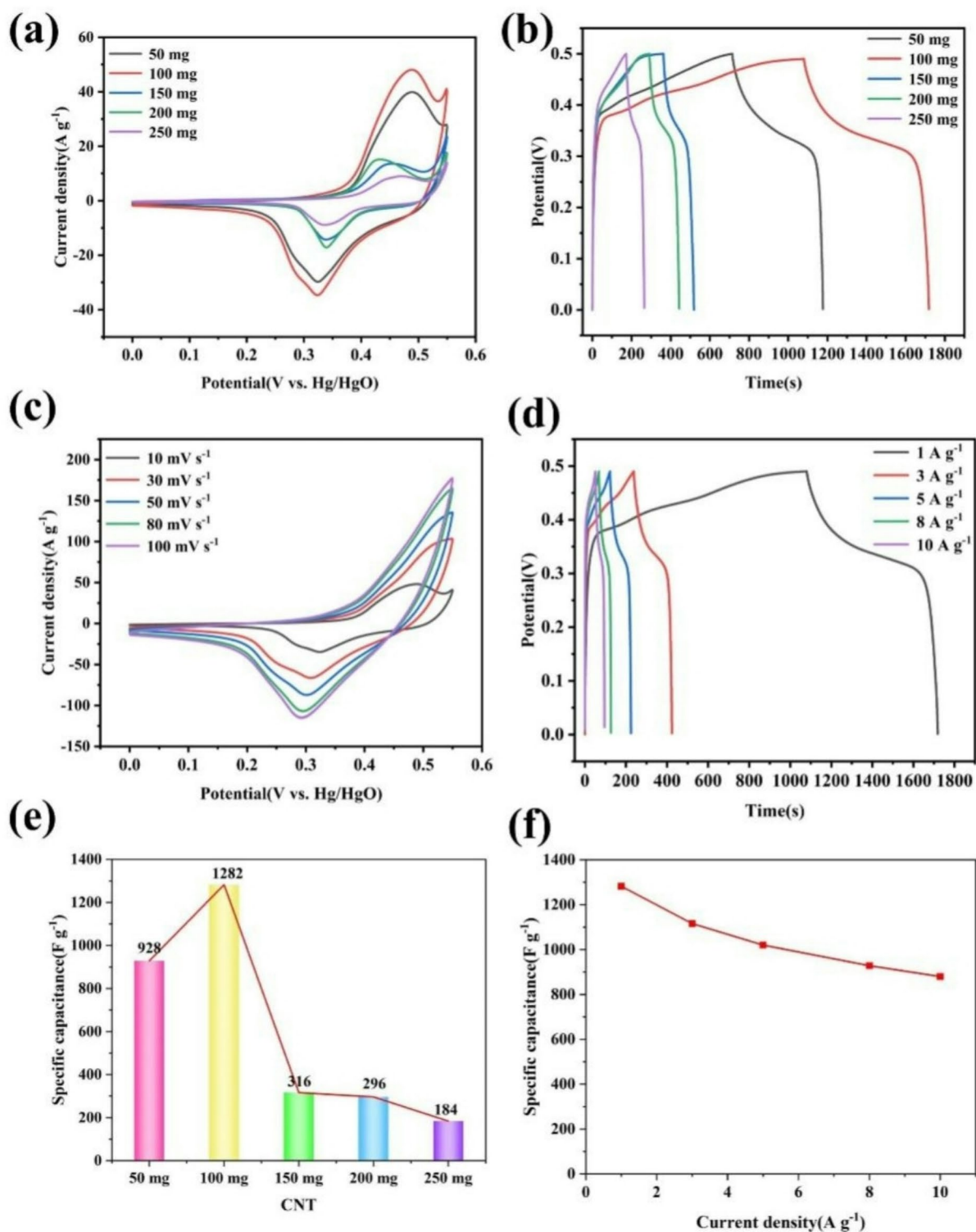
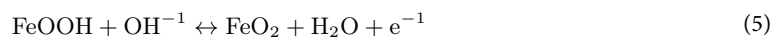
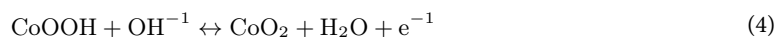
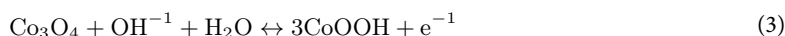
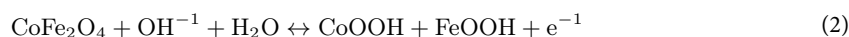


Fig. 5. (a) CV curves of FCO@CNTs with different mass of CNTs at the scanning rate of 10 mV s⁻¹; (b) GCD curves of FCO@CNTs with different mass of CNTs at a current density of 1 A g⁻¹; (c) CV curves of FCO@CNT-100 at various scanning rates; (d) GCD curves of FCO@CNT-100 at various current densities; (e) Specific capacitance of FCO@CNT-100 at a current density of 1 A g⁻¹; (f) Specific capacitance of FCO@CNT-100 at various current densities.



Among the synthesized FCO@CNTs composites, FCO@CNT-100 exhibited the most pronounced redox peaks and the largest integral area under the cyclic voltammetry (CV) curves, indicating the highest specific capacitance. Figure 5b presents the galvanostatic charge–discharge (GCD) curves of the FCO@CNTs composites at a current density of 1 A g⁻¹. In this study, the voltage window for FCO@CNT-100 was established at 0.49 V, a decision influenced by the intrinsic electrochemical properties as well as the structural and compositional attributes of the material^{53–58}. Notably, FCO@CNT-100 demonstrated the longest discharge time and the highest specific capacitance (641 C g⁻¹) (as shown in Fig. 5e), corresponding with the results from the CV studies. These results suggest that an optimal mass of 100 mg of CNTs is crucial for achieving the best performance, while an excess may result in CNT agglomeration and a disproportionately high contribution from double-layer capacitance. However, when compared to CoFe-ZIF@CNTs, FCO@CNTs displayed superior specific capacitance, which can be ascribed to the beneficial effect of the transition metal oxide component. Figure 5c depicts the CV curves of FCO@CNT-100 at varying scan rates. The magnitude of the redox current increases in conjunction with the scanning velocity, and it is capable of maintaining the CV curve within the same general configuration consistently. The oxidation and reduction peaks exhibit a slight shift towards more positive and negative potentials, respectively, which is indicative of the electrode's superior electrical conductivity and exceptional rate performance. The peak at 0.55 V during the oxidation process can be attributed to polarization phenomena. Such emergence of polarization is likely due to the relatively low potential of the metal ions of Co³⁺ and Fe³⁺, which exhibit a more reactive response beyond this voltage threshold. The shape of the CV curves suggests that the electrode exhibits characteristic pseudocapacitive behavior, distinct from the more typical, nearly rectangular shape associated with bilayer capacitance. A rapid and reversible redox reaction at the electrode–electrolyte interface results in a peak current that increases sharply with the scan rate, signifying efficient electron and ion transfer kinetics⁵⁹. Figure 5d shows the GCD curves of FCO@CNT-100 at different current densities. Employing the formula (1), the specific capacitance of FCO@CNT-100 at a current density of 10 A g⁻¹ was calculated to be 440 C g⁻¹, with a capacitance retention of 69% when current density decreased to 1 A g⁻¹ (Fig. 5f). The electrochemical capacitance of the FCO@CNT-100 electrode is derived almost entirely from the active material. After 5000 cycles at a current density of 10 A g⁻¹, FCO@CNT-100 maintained a commendable capacitance retention of 62.3% (as detailed in Fig. S4). The SEM image of the FCO@CNT-100 electrode material after 5000 cycles of charge–discharge testing is depicted in Fig. S5. It can be observed that the electrode material maintains its spherical morphology even after 5000 cycles of cyclic testing. In comparison to other samples, FCO@CNT-100 not only achieved the highest specific capacitance but also demonstrated excellent rate capability and cycling stability. As shown in Table S4, in comparison to CNT-based supercapacitor electrode materials previously reported (specific capacitance varying from 29.78 C g⁻¹ to 532.2 C g⁻¹ at a current density of 1 A g⁻¹), the electrode material synthesized in the present study demonstrates enhanced specific capacitance (641 C g⁻¹ at a current density of 1 A g⁻¹) and superior rate performance (69% at a current density of 10 A g⁻¹). This improvement is likely attributed to the synergistic effect of the multi-metallic components within the synthesized porous network structure (spherical CoFe₂O₄@Co₃O₄ and carbon nanotubes), coupled with the material's large specific surface area (309.929 m²/g).

The electrochemical performance of electrode materials is significantly influenced by their specific surface area and pore size distribution, as these attributes determine the accessibility of active sites. While larger pores may facilitate rapid ion transport, they can also lead to incomplete utilization of active sites, thereby reducing overall efficiency. These characteristics were assessed through nitrogen adsorption–desorption isotherms at a temperature of 77 K. The results for FCO@CNT-100 are illustrated in Fig. S6. FCO@CNT-100 exhibited the typical Type IV isotherm behavior, signifying the presence of mesoporous structures, as observed in Fig. S6(a). The presence of H3 hysteresis loops within the isotherms suggests that the material possesses slit-like or wedge-like pores. This confirmed porosity is a crucial attribute for enhancing electrochemical activity. Surface area analysis via the Brunauer–Emmett–Teller (BET) method indicated that FCO@CNT-100 possesses a surface area of 309.929 m²/g. Additionally, the average pore diameter for FCO@CNT-100 was determined to be 16.848 nm, as depicted in Fig. S6(b). Given its large specific surface area, FCO@CNT-100 can offer an increased number of active sites during electrochemical processes, effectively enhancing its specific capacitance.

Electrochemical impedance spectroscopy (EIS) was conducted on the synthesized samples at the open circuit potential, with a frequency range spanning from 0.01 Hz to 100 kHz. The corresponding Nyquist plots for the FCO@CNTs samples are presented in Fig. S7(a). In the high-frequency region, the point of intersection of the plot with the real axis (X-axis) on the Nyquist diagram is indicative of the internal resistance (R_s) of the electrode. The semicircular arc observed in the Nyquist plots at high frequencies corresponds to the charge transfer resistance (R_{ct}) of the electrode, with the arc's diameter reflecting the magnitude of the R_{ct} . The inclined line at low frequencies represents the Warburg impedance, which is associated with proton diffusion within the electrode material and the diffusion resistance imposed by the electrolyte, as documented in the literature^{60,61}. It is observed that the R_{ct} values for the FCO@CNTs samples are 0.78, 0.7, 0.81, 0.87, and 0.84 Ω, respectively (Fig. S7(b)). Notably, FCO@CNT-100 exhibits the lowest R_{ct} of 0.7 Ω, signifying the smallest internal resistance and highest electron conductivity among the samples. These results suggest that the synergistic effect of incorporating carbon nanotubes (100 mg) and the substitutional doping with Co²⁺/Co³⁺ and Fe²⁺/Fe³⁺ ions can enhance the electron conductivity of the active material components⁶². As depicted in Fig. S8, the EIS image of FCO@CNT-

100 is presented following 5000 cycles. It is observable from the figure that there is no significant alteration in the impedance of the electrode material before and after the cycling process.

The specific capacitance of electrode materials are dictated by interfacial capacitance and diffusion-controlled capacitance, with the latter's process being reliant on the diffusion coefficient. The Randles–Sevcik equation serves to quantify this relationship as follows⁶³:

$$j_p = 0.4463v^{\frac{1}{2}} \frac{z^{\frac{1}{2}} n^{\frac{3}{2}} F^{\frac{3}{2}}}{R^{\frac{1}{2}} T^{\frac{1}{2}}} \quad (6)$$

In the given formula, " v " (mV s^{-1}) denotes the scanning rate, " n " represents the number of electrons participating in the redox process, " F " symbolizes the Faraday constant, " R " is the gas constant, " T " signifies the absolute temperature, and " c_0 " refers to the initial concentration of electrons available for extraction within the material. The diffusion coefficient is directly proportional to the slope of the linear relationship between the peak current densities for oxidation/reduction and the square root of the scanning rate ($v^{1/2}$). A steeper slope is indicative of a larger diffusion coefficient, which underscores a more pronounced diffusion control mechanism. As depicted in Fig. 6a–e, the linear regressions for the FCO@CNTs samples are presented, revealing that FCO@CNT-100 has the steepest slope. This observation suggests that FCO@CNT-100 exhibits the most significant diffusion control influence.

The following equations are employed to analyze kinetic behavior of electrode materials during an electrochemical reaction⁶⁰:

$$i = av^b \quad (7)$$

$$\log i = b \log v + a \quad (8)$$

Within the framework where v (mV s^{-1}) signifies the scan rates and i represents the current of the oxidation/reduction peaks, the parameter b is indicative of the charge storage dynamics of the electrode materials⁶⁴ (a) A b value of 0.5 suggests that the materials operate as battery-type electrodes, with capacitance predominantly governed by diffusion processes. (b) If b lies between 0.5 and 1, it indicates that the electrode material's capacitance arises from a combination of diffusion processes and interfacial capacitance^{64,65}. (c) A b value of 1 or greater implies that the electrode capacitance is predominantly influenced by interfacial capacitance. As shown in Fig. 6f, the b values for FCO@CNT-100 are 0.5716 for oxidation and 0.5273 for reduction peaks. These values demonstrate that the electrode material exhibits both battery-like and pseudo-capacitive behaviors. This indicates a synergistic interplay between faradaic redox reactions (characterized by reversible ion intercalation/deintercalation) and rapid surface adsorption/desorption processes, which are hallmarks of pseudo-capacitance which together contribute to the enhanced electrochemical performance of FCO@CNT-100 and enhance specific capacitance but can also result in incomplete charge transfer and lower energy efficiency. Moreover, the significant drop in capacitance at higher current densities indicates rate-dependent behavior, which is a contributing factor to the lower energy efficiency.

The contribution of diffusion process and interface capacity to capacitance can be analyzed by the equation^{64–66}:

$$\frac{I}{v^{0.5}} = k_1 v + k_2 \quad (9)$$

In this context, I denotes the current in amperes (A), v represents the scan rate, and k_1 and k_2 are constants. Figure 7 illustrates the distinct contributions of the diffusion process and the interfacial capacitance to the electrochemical performance of FCO@CNT-100 across a range of scanning rates. It is observed that as the scanning rate increases, the influence of interfacial capacitance becomes increasingly significant. This pronounced capacitive effect is likely attributable to ions encountering shorter diffusion pathways and the material's efficient electronic transport properties. These findings further corroborate that at higher scanning rates, the charge storage behavior of FCO@CNT-100 is predominantly governed by surface-confined redox reactions.

Conclusion

To sum up, the fabrication of the FCO@CNT-100 three-dimensional (3D) porous network has been successfully synthesized through a combination of hydrothermal synthesis followed by calcination. The strategic architectural design of FCO@CNT-100 facilitates an abundance of active sites and ion-transport pathways, which enhances ion and electron mobility during electrochemical reactions. This enhancement is beneficial for improving the interfacial contact between the electrodes and the electrolyte. Consequently, the FCO@CNT-100 electrodes have demonstrated superior electrochemical performance. Notably, at a current density of 1 A g^{-1} , the specific capacitance of FCO@CNT-100 reached a significant value of 641 C g^{-1} , and it retained approximately 69% of this capacitance upon a tenfold increase in current density to 10 A g^{-1} . Furthermore, after 5000 cycles at a high current density of 10 A g^{-1} , the FCO@CNT-100 exhibited a capacitance retention of 62.3%. The systematic methodology employed in this study for the synthesis of the FCO@CNT-100 3D porous network provides a potentially effective paradigm for the development of advanced hybrid electrode materials for supercapacitor applications. The electrode material for the supercapacitor designed in this study possesses a larger specific surface area and better cyclic stability, which is expected to enhance the performance of the supercapacitor. It has the potential for application in the fields of renewable energy storage systems, electric vehicles, and portable electronic device.

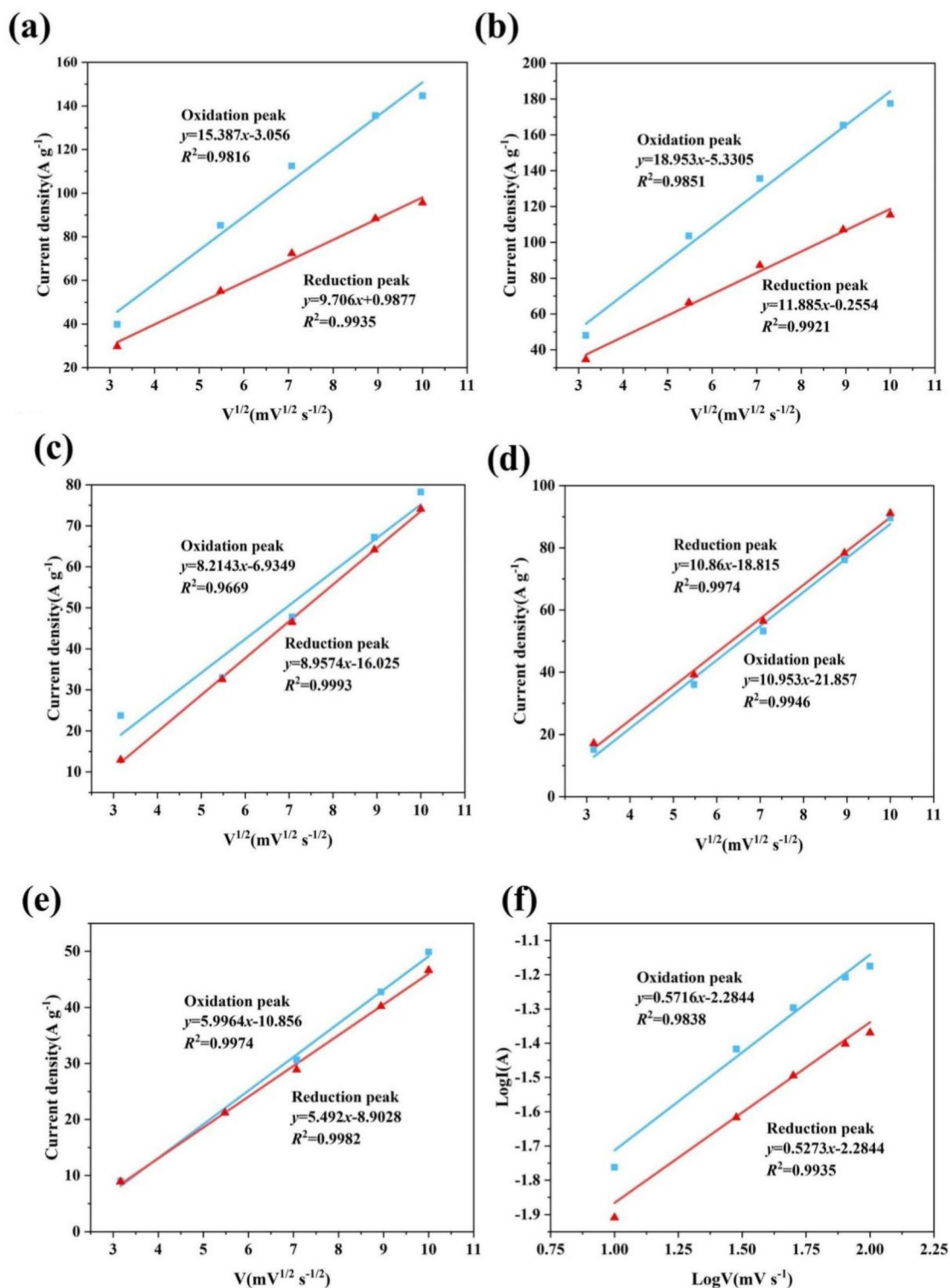


Fig. 6. The plots of I and $V^{1/2}$: (a) FCO@CNT-50; (b) FCO@CNT-100; (c) FCO@CNT-150; (d) FCO@CNT-200; (e) FCO@CNT-250; (f) The plot of $\text{Log} I$ and $\text{Log} V$ of FCO@CNT-100.

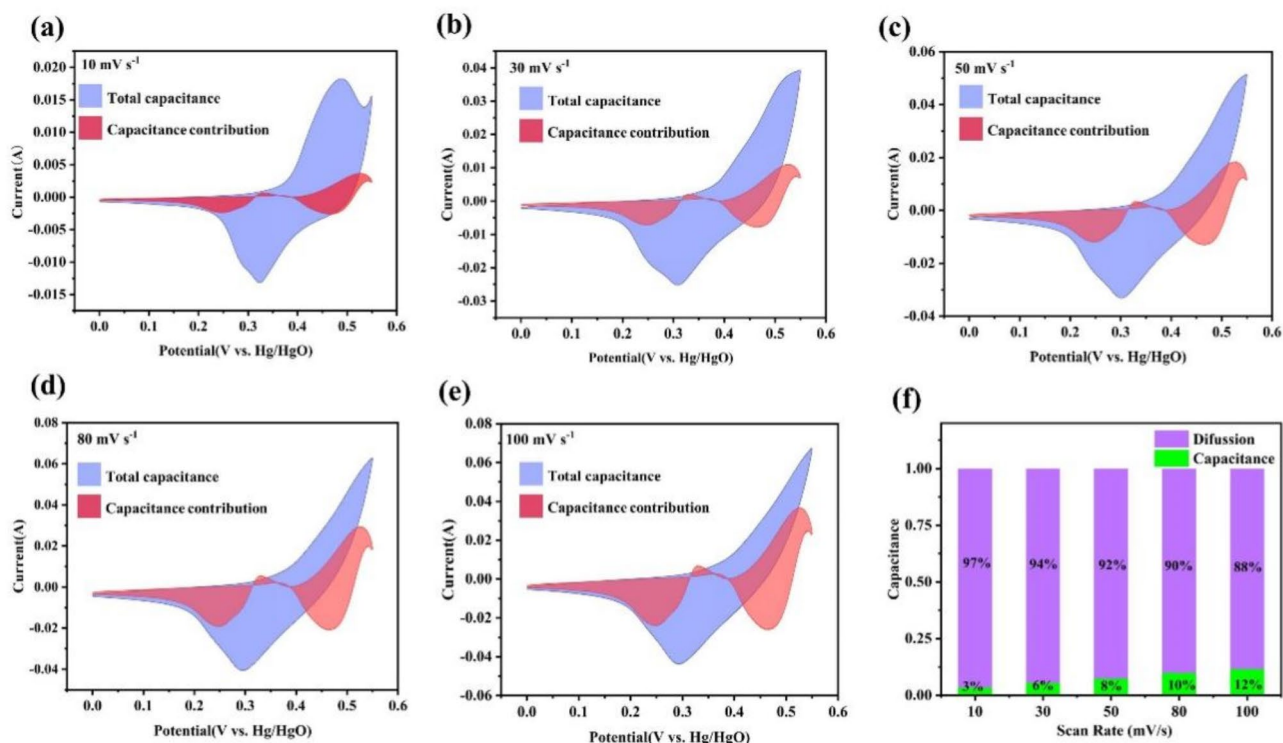


Fig. 7. Surface contribution and capacitance contribution of FCO@CNT-100 at various scanning rates: (a) 10 mV s⁻¹; (b) 30 mV s⁻¹; (c) 50 mV s⁻¹; (d) 80 mV s⁻¹ (e) 100 mV s⁻¹ (f) The contribution of capacitance and diffusion.

Data availability

Data is provided within the manuscript or supplementary information files, if there are any problems, please contact the corresponding author, Dr. Wu (1361087131@qq.com).

Received: 29 December 2024; Accepted: 26 February 2025

Published online: 10 July 2025

References

- Zhang, C. et al. Investigation on the energy storage performance of Cu₂Se@ MnSe heterojunction hollow spherical shell for aluminum-ion battery. *Chem. Eng. J.* **474**, 145688 (2023).
- Wang, L. et al. High-rate and long cycle-life alloy-type magnesium-ion battery anode enabled through (De) magnesiation-induced near-room-temperature solid-liquid phase transformation. *Adv. Energy Mater.* **9**(45), 1902086 (2019).
- Tay, I. R., Xue, J. & Lee, W. S. V. Methods for characterizing intercalation in aqueous zinc ion battery cathodes: A review. *Adv. Sci.* **10**(26), 2303211 (2023).
- Wu, Z. et al. Engineering high conductive Li⁷P₂S₈I via Cl⁻ doping for all-solid-state Li-S batteries workable at different operating temperatures. *Chem. Eng. J.* **442**, 136346. <https://doi.org/10.1016/j.cej.2022.136346> (2022).
- Wu, Z. et al. AgPF₆ modified lithium interphases enable superior performance for Li_{1.5}PS_{4.5}Cl_{1.5}-based all-solid-state lithium metal batteries. *J. Power Sources* **602**, 234295. <https://doi.org/10.1016/j.jpowsour.2024.234295> (2024).
- Wu, Z. et al. Enhancing solid-state lithium metal battery performance via indium-based modification of electrolytes and lithium metal surfaces: mechanistic insights and optimization. *Sci. China Chem.* **68**, 1144–1158. <https://doi.org/10.1007/s11426-024-2275-2> (2025).
- Wu, Z. et al. Ag-modification argyrodite electrolytes enable high-performance for all-solid-state lithium metal batteries. *Chem. Eng. J.* **466**, 143304. <https://doi.org/10.1016/j.cej.2023.143304> (2023).
- Cevher, D. et al. Enhancing electrochromic supercapacitor electrode performance through different donor compartments in DAD type conjugated polymers. *J. Energy Storage* **74**, 109501 (2023).
- Xiong, C. et al. Non-carbonized porous lignin-free wood as an effective scaffold to fabricate lignin-free Wood@ Polyaniline supercapacitor material for renewable energy storage application. *J. Power Sources* **471**, 228448 (2020).
- Joshi, B. et al. Review of recent progress in electrospinning-derived freestanding and binder-free electrodes for supercapacitors. *Coord. Chem. Rev.* **460**, 214466 (2022).
- Qin, T. et al. Flexible and wearable all-solid-state supercapacitors with ultrahigh energy density based on a carbon fiber fabric electrode. *Adv. Energy Mater.* **7**(20), 1700409 (2017).
- Salanne, M. et al. Efficient storage mechanisms for building better supercapacitors. *Nat. Energy* **1**(6), 1–10 (2016).
- Lin, Z. et al. Materials for supercapacitors: When Li-ion battery power is not enough. *Mater. today* **21**(4), 419–436 (2018).
- Xu, J. et al. A hierarchical carbon derived from sponge-templated activation of graphene oxide for high-performance supercapacitor electrodes. *Adv. Mater.* **28**(26), 5222–5228 (2016).
- El-Kady, M. F., Shao, Y. & Kaner, R. B. Graphene for batteries, supercapacitors and beyond. *Nat. Rev. Mater.* **1**(7), 1–14 (2016).
- Mao, X. et al. Three-dimensional self-supporting Ti₃C₂ with MoS₃ and Cu₂O nanocrystals for high-performance flexible supercapacitors. *ACS Appl. Mater. Interfaces* **13**(19), 22664–22675 (2021).

17. Zeng, J. et al. Split-cell symmetric supercapacitor performance of bimetallic MOFs yolk-shell hierarchical microstructure. *Mater. Lett.* **309**, 131305 (2022).
18. Hu, L., Chen, W. & Xie, X., et al. Symmetrical MnO₂-carbon nanotube-textile nanostructures for wearable pseudocapacitors with high mass loading. *ACS Nano* **5**(11), 8904–8913 (2011).
19. Chodankar, N. R. et al. Dendritic nanostructured waste copper wires for high-energy alkaline battery. *Nano-Micro Lett.* **12**, 1–12 (2020).
20. Ma, Y. et al. Photoactive manganese ferrite-modified bacterial anode to simultaneously boost both mediated and direct electron transfer processes in microbial fuel cells. *ACS Sustain. Chem. Eng.* **10**(10), 3355–3362 (2022).
21. Arun, T. et al. NiFe₂O₄ nanospheres with size-tunable magnetic and electrochemical properties for superior supercapacitor electrode performance. *Electrochim. Acta* **399**, 139346 (2021).
22. Rani, B. & Sahu, N. K. Electrochemical properties of CoFe₂O₄ nanoparticles and its rGO composite for supercapacitor. *Diam. Relat. Mater.* **108**, 107978 (2020).
23. Chodankar, N. R. et al. Solution-free self-assembled growth of ordered tricopper phosphide for efficient and stable hybrid supercapacitor. *Energy Storage Mater.* **39**, 194–202 (2021).
24. Patil, S. J. et al. Ultra-stable flexible Zn-ion capacitor with pseudocapacitive 2D layered niobium oxyphosphides. *Energy Storage Mater.* **45**, 1040–1051 (2022).
25. Mandal, S. & Dasmahapatra, A. K. Hierarchical polyaniline/copper cobalt ferrite nanocomposites for high performance supercapacitor electrode. *J. Energy Storage* **74**, 109402 (2023).
26. Mahmoud, M. H., Elshahawy, A. M. & Taha, T. A. Lithium dopant assisted surface modification Zn ferrites for high-performance supercapacitor applications. *J. Energy Storage* **68**, 107881 (2023).
27. Lashkenari, M. S. et al. Facile synthesis of N-doped graphene oxide decorated with copper ferrite as an electrode material for supercapacitor with enhanced capacitance. *Electrochim. Acta* **465**, 142959 (2023).
28. Naseri, M. G. et al. Simple synthesis and characterization of cobalt ferrite nanoparticles by a thermal treatment method. *J. Nanomater.* **2010**, 1–8 (2010).
29. Tahernejad-Javazmi, F., Shabani-Nooshabadi, M. & Karimi-Maleh, H. 3D reduced graphene oxide/FeNi³⁺ ionic liquid nanocomposite modified sensor; an electrical synergic effect for development of tert-butylhydroquinone and folic acid sensor. *Compos. Part B Eng.* **172**, 666–670 (2019).
30. Patil, A. M. et al. Interior design engineering of CuS architecture alteration with rise in reaction bath temperature for high performance symmetric flexible solid state supercapacitor. *J. Ind. Eng. Chem.* **46**, 91–102 (2017).
31. Wang, M. X. et al. ZIF-67 derived Co₃O₄/carbon aerogel composite for supercapacitor electrodes. *N. J. Chem.* **43**(15), 5666–5669 (2019).
32. Wang, S. X. et al. Nickel-molybdenum metal hydroxide wrapped ZIF-67 for supercapacitor applications. *J. Energy Storage* **59**, 106555 (2023).
33. Thanh, T. D. et al. Recent advances in two-dimensional transition metal dichalcogenides-graphene heterostructured materials for electrochemical applications. *Prog. Mater. Sci.* **96**, 51–85 (2018).
34. Reddy, P. A. K. et al. Synthesis of ZIF-67-derived CoS₂@graphitic carbon/reduced graphene oxide for supercapacitor application. *Chem. Eng. J.* **471**, 144608 (2023).
35. Choi, J. et al. Fluoride ion-mediated morphology control of fluorine-doped CoFe₂O₄/graphene sheet composites for hybrid supercapacitors with enhanced performance. *Electrochim. Acta* **279**, 241–249 (2018).
36. Liu, K. et al. A self-supported graphene/carbon nanotube hollow fiber for integrated energy conversion and storage. *Nano-Micro Lett.* **12**, 1–11 (2020).
37. Liu, K. et al. Textile-like electrodes of seamless graphene/nanotubes for wearable and stretchable supercapacitors. *J. Power Sources* **446**, 227355 (2020).
38. Islam, M. S., Shudo, Y. & Hayami, S. Energy conversion and storage in fuel cells and super-capacitors from chemical modifications of carbon allotropes: State-of-art and prospect. *Bull. Chem. Soc. Jpn.* **95**(1), 1–25 (2022).
39. Zhang, S. et al. Carbon-nanotube-based electrical conductors: Fabrication, optimization, and applications. *Adv. Electron. Mater.* **5**(6), 1800811 (2019).
40. Chodankar, N. R. et al. True meaning of pseudocapacitors and their performance metrics: Asymmetric versus hybrid supercapacitors. *Small* **16**(37), 2002806 (2020).
41. Cheng, X. et al. Hierarchically core-shell structured nanocellulose/carbon nanotube hybrid aerogels for patternable, self-healing and flexible supercapacitors. *J. Colloid Interface Sci.* **660**, 923–933 (2024).
42. Mashkoo, F. et al. CNT supported Sm/Co-LDH for antimony adsorption and subsequent application in supercapacitor to prevent secondary pollution. *J. Alloys Compd.* **981**, 173557 (2024).
43. Zhang, G. et al. Preparation and mechanism investigation of walnut shell-based hierarchical porous carbon for supercapacitors. *Bull. Chem. Soc. Jpn.* **96**(3), 190–197 (2023).
44. Li, Y. et al. Sulfur and nitrogen Co-doped activated CoFe₂O₄@C nanotubes as an efficient material for supercapacitor applications. *Carbon* **162**, 132–154 (2020).
45. Zhang, Y. & Park, S. J. Formation of hollow MoO₃/SnS₂ heterostructured nanotubes for efficient light-driven hydrogen peroxide production. *J. Mater. Chem. A* **6**, 20304–20312 (2018).
46. Shuai, C. et al. A combined nanostructure constructed by graphene and boron nitride nanotubes reinforces ceramic scaffolds. *Chem. Eng. J.* **313**, 487–549 (2017).
47. Xiong, W. et al. Construction of porous NiCo₂S₄ hierarchical nanoflakes based on zeolitic imidazolate frameworks as battery-type electrodes for high performance supercapacitors. *J. Energy Storage* **47**, 103583 (2022).
48. Xu, R. et al. A two-step hydrothermal synthesis approach to synthesize NiCo₂S₄/NiS hollow nanospheres for high-performance asymmetric supercapacitors. *Appl. Surf. Sci.* **422**, 597–606 (2017).
49. Abbasi, L., Arvand, M. & Moosavifard, S. E. Facile template-free synthesis of 3D hierarchical ravine-like interconnected MnCo₂S₄ nanosheet arrays for hybrid energy storage device. *Carbon* **161**, 299–308 (2020).
50. Cai, X. et al. Solvothermal synthesis of NiCo-layered double hydroxide nanosheets decorated on RGO sheets for high performance supercapacitor. *Chem. Eng. J.* **268**, 251–259 (2015).
51. Acharya, J. et al. Facile one pot sonochemical synthesis of CoFe₂O₄/MWCNTs hybrids with well-dispersed MWCNTs for asymmetric hybrid supercapacitor applications. *Int. J. Hydrog. Energy* **45**(4), 3073–3085 (2020).
52. Yang, S. et al. Oxygen-vacancy abundant ultrafine Co₃O₄/graphene composites for high-rate supercapacitor electrodes. *Adv. Sci.* **5**(4), 1700659 (2018).
53. Wei, D. et al. CNT/Co₃S₂@NiCo LDH ternary nanocomposites as battery-type electrode materials for hybrid supercapacitors. *J. Alloys Compd.* **824**, 153937 (2020).
54. Yao, M. et al. Self-standing ultrathin NiCo₂S₄@carbon nanotubes and carbon nanotubes hybrid films as battery-type electrodes for advanced flexible supercapacitors. *J. Power Sources* **543**, 231829 (2022).
55. Wang, Y. et al. Facile construction of Co(OH)₂@Ni(OH)₂ core-shell nanosheets on nickel foam as three dimensional free-standing electrode for supercapacitors. *Electrochim. Acta* **293**, 40–46 (2019).
56. Li, Y. et al. Controllable synthesis of NiCo₂O₄/CNT composites for supercapacitor electrode materials. *Int. J. Electrochem. Sci.* **15**(11), 11567–11583 (2020).

57. Peçenek, H. et al. Highly compressible binder-free sponge supercapacitor electrode based on flower-like NiO/MnO₂/CNT. *J. Alloys Compd.* **913**, 165053 (2022).
58. Raj, B. G. S. et al. A novel Fe₂O₃-decorated N-doped CNT porous composites derived from tubular polypyrrole with excellent rate capability and cycle stability as advanced supercapacitor anode materials. *Electrochim. Acta* **334**, 135627 (2020).
59. Zheng, J. & Bai, X. Preparation of Ni-Co PBA-derived beaded NiSe₂/CoSe₂/CNT for high-performance supercapacitors. *J. Alloys Compd.* **944**, 169110 (2023).
60. Guo, C. et al. Approach of fermi level and electron-trap level in cadmium sulfide nanorods via molybdenum doping with enhanced carrier separation for boosted photocatalytic hydrogen production. *J. Colloid Interface Sci.* **583**, 661–671 (2021).
61. Niu, H. et al. NiCo-layered double-hydroxide and carbon nanosheets microarray derived from MOFs for high performance hybrid supercapacitors. *J. Colloid Interface Sci.* **539**, 545–552 (2019).
62. Ma, Z. et al. Carbon nanotubes interpenetrating MOFs-derived Co-Ni-S composite spheres with interconnected architecture for high performance hybrid supercapacitor. *J. Colloid Interface Sci.* **602**, 627–635 (2021).
63. Churikov, A. V. et al. Kinetics of electrochemical lithium intercalation into thin tungsten (VI) oxide layers. *Russ. J. Electrochem.* **44**, 530–542 (2008).
64. Liu, Y. et al. 3D CNTs/graphene network conductive substrate supported MOFs-derived CoZnNiS nanosheet arrays for ultra-high volumetric/gravimetric energy density hybrid supercapacitor. *J. Colloid Interface Sci.* **583**, 288–329 (2021).
65. Ilayas, T. et al. Rietveld refinement, 3D view and electrochemical properties of rare earth lanthanum doped nickel ferrite to fabricate high performance electrodes for supercapacitor applications. *Ceram. Int.* **49**, 28864 (2023).
66. Li, C., Ma, D. & Zhu, Q. ZIF-67 derived Co₂VO₄ hollow nanocubes for high performance asymmetric supercapacitors. *Nanomaterials* **12**(5), 848 (2022).

Acknowledgements

This work was financially supported by the Key Research and Key Projects Foundation of Jiangxi Province (20212BBE51013), the Foundation of National Laboratory of Solid-State Microstructures (M35026), the National Natural Science Foundation of China (Grant No. 52061030, 11604147), and the “shuangqian” program (jxsq2019101047) of Jiangxi province.

Author contributions

Xiaojun Ding: Conceptualization, Data curation, Investigation, Writing—original draft. Dingbang Liu: Methodology, Data curation, Investigation, Writing—original draft. Zihao Wang: Methodology, Formal analysis. Yilin Peng: Methodology, Formal analysis. Shuqi Fu: Investigation, Formal analysis. Na Zhan: Formal analysis, Writing—review & editing. Qing Jiang: Conceptualization, Formal analysis, Investigation, Writing—review & editing, Supervision. Mingyang Li: Conceptualization, Formal analysis, Investigation, Writing—review & editing, Supervision. Haiyang Wan: Conceptualization, Formal analysis, Investigation, Writing—review & editing, Supervision. Jiansheng Liu: Conceptualization, Formal analysis, Investigation, Writing—review & editing, Supervision. Xincheng Zhao: Conceptualization, Formal analysis, Investigation, Writing—review & editing, Supervision. Fei Gao: Conceptualization, Formal analysis, Investigation, Writing—review & editing, Supervision. Weiping Zhou: Conceptualization, Formal analysis, Investigation, Writing—review & editing, Supervision. Zhenzhi Cheng: Conceptualization, Formal analysis, Investigation, Writing—review & editing, Supervision. Zhongkai Wu: Conceptualization, Formal analysis, Investigation, Writing—review & editing, Supervision. Guangsheng Luo: Conceptualization, Formal analysis, Investigation, Writing—review & editing, Supervision. All authors reviewed the manuscript.

Declarations

Competing interests

The authors declare no competing interests.

Additional information

Supplementary Information The online version contains supplementary material available at <https://doi.org/10.1038/s41598-025-92302-3>.

Correspondence and requests for materials should be addressed to X.Z., F.G., Z.W. or G.L.

Reprints and permissions information is available at www.nature.com/reprints.

Publisher's note Springer Nature remains neutral with regard to jurisdictional claims in published maps and institutional affiliations.

Open Access This article is licensed under a Creative Commons Attribution-NonCommercial-NoDerivatives 4.0 International License, which permits any non-commercial use, sharing, distribution and reproduction in any medium or format, as long as you give appropriate credit to the original author(s) and the source, provide a link to the Creative Commons licence, and indicate if you modified the licensed material. You do not have permission under this licence to share adapted material derived from this article or parts of it. The images or other third party material in this article are included in the article's Creative Commons licence, unless indicated otherwise in a credit line to the material. If material is not included in the article's Creative Commons licence and your intended use is not permitted by statutory regulation or exceeds the permitted use, you will need to obtain permission directly from the copyright holder. To view a copy of this licence, visit <http://creativecommons.org/licenses/by-nc-nd/4.0/>.

© The Author(s) 2025